Journal of
Materials Chemistry A

Phytic Acid Induced Nitrogen Configuration Adjustment of Active Nitrogen-Rich Carbon Nanosheets for High-Performance Potassium-Ion Storage

Journal Name

ARTICLE

Phytic Acid Induced Nitrogen Configuration Adjustment of Active Nitrogen-Rich Carbon Nanosheets for High-Performance Potassium-Ion Storage

Liang Ma[1a], Zhibin Li[1a], Jinliang Li*[a], Yao Dai[b], Chen Qian[c], Yaofeng Zhu[c], Hao Wang[d], Kwun Nam Hui[e], Likun Pan[f], Mohammed A. Amin[g], Yusuke Yamauchi*[h,i] and Wenjie Mai*[a]

As a conventional modification approach, nitrogen doping in carbon can greatly improve the electrochemical performance for potassium (K)-ion storage. However, we realized that the improvement of electrochemical performance by simple nitrogen doping alone in carbon was not as good as we expected. In this work, we develop a new approach to design active nitrogen-rich carbon nanosheets (PANC) by phytic acid induction, which present a remarkable improvement specific capacity of 317 mAh g^{-1} after 100 cycles at 50 mA g^{-1} and 202 mAh g^{-1} at 500 mA g^{-1} even after 3200 cycles. Density functional theory (DFT) calculations confirm the increased pyridinic-N as active sites contributes to the enhancement of K-ion adsorption ability. In addition, our calculation illustrates that pyridinic-N displays a smaller energy barrier of 0.16 eV compared to that of 1.12 eV for pyrrolic-N, indicating that pyridinic-N in carbon is the critical factor to improve the K-ion storage performance for our PANCs. This result is also confirmed by the electrochemical impedance spectroscopy and pseudocapacitance analysis. We believe that our work develops an effective approach to realize the active N adjustment, which will inspire the design of high-performance anode materials for potassium ion storage.

1. Introduction

As the primary choice for prospective anode materials of potassium (K)-ion storage, carbon materials have drawn extensive interests.[1-7] However, conventional carbon materials always exhibit low specific capacity, which cannot meet the

a. Siyuan Laboratory, Guangzhou Key Laboratory of Vacuum Coating Technologies and New Energy Materials, Guangdong Provincial Engineering Technology Research Center of Vacuum Coating Technologies and New Energy Materials, Department of Physics, Jinan University, Guangzhou 510632, China.
b. School of Materials and Guangdong Engineering Technology Research Centre for Advanced Thermal Control Material and System Integration (ATCMSI), Sun Yat-sen University, Guangzhou 510275, P. R. China.
c. School of Materials Science and Engineering, Zhejiang Sci-Tech University, Hangzhou, Zhejiang 310018, China.
d. Guangdong Provincial Key Laboratory of Micro/Nano Optomechatronics Engineering, College of Mechatronics and Control Engineering, Shenzhen University, Shenzhen, 518060 China.
e. Institute of Applied Physics and Materials Engineering (IAPME), University of Macau. Department of Physics and Chemistry, Faculty of Science and Technology, University of Macau, Macao SAR 999078.
f. Shanghai Key Laboratory of Magnetic Resonance, School of Physics and Electronic Science, East China Normal University, Shanghai 200241, China.
g. Department of Chemistry, College of Science, Taif University, Taif 21944, Saudi Arabia
h. School of Chemical Engineering and Australian Institute for Bioengineering and Nanotechnology (AIBN), The University of Queensland, Brisbane, QLD 4072, Australia
i. JST-ERATO Yamauchi Materials Space-Tectonics Project and International Center for Materials Nanoarchitectonics (WPI-MANA), National Institute for Materials Science (NIMS), Namiki 1-1, Tsukuba, Ibaraki 305-0044, Japan
1 These two authors contributed equally to this work.
*Corresponding author: lijinliang@email.jnu.edu.cn (Jinliang Li); y.yamauchi@uq.edu.au (Yusuke Yamauchi); wenjiemai@email.jnu.edu.cn (Wenjie Mai)

demand of K-ion batteries (KIBs). To improve the electrochemical performance of carbon-based materials for KIBs, scientists first raised those doping heteroatoms into the carbon materials can remarkably enhance the K-ion storage performance.[8-13] Among all the heteroatoms doping, nitrogen (N) doping is considered to be an effective way to acquire the high performance in KIBs, which has been widely demonstrated in previous works.[14-19] In spite of these works, they mainly proved that N doping could improve the performance of K-ion storage, which is due to the enhancement of the adsorption energy after N doping. In fact, the regulation of reactive N from atomic level still lacks deeply involvement. According to some reports, they found that the doping N configuration mainly was constituted by pyridinic-N, pyrrolic-N, oxidized-N and graphitic-N. The N configuration always has an important impact on the performance improvement and the content of active-N in N-doped carbon might be the key parameter to determine the K-ion storage performance.[20-22] However, further demonstrating the effect of N-configuration for K-ion storage and seeking an appropriate approach to increase the active N content in N-doped carbon are still great challenge in KIB's field.

In our work, we compare the adsorption energies (ΔE_a) of different N-configuration for K-ion adsorption and find that the pyridinic-N presents more negative ΔE_a by density functional theory (DFT) calculations, which confirms that the increased pyridinic-N contributes to the enhancement of K-ion adsorption ability. Otherwise, we are aware of that phytic acid (PA) can provide the active P atoms, leading to high distortion of carbon structures, which contributes to the open edge sites to form

active-N.[23-25] Herein, we attempt to use PA as inductive agent to realize the design of high proportion of active-N carbon nanosheets (PANC). From the characterizations, it is found that the type of doped-N configuration can be changed with regulated PA. With the increase of the content of pyridinic-N, our PANC presents a remarkable improvement specific capacity of 317 mAh g^{-1} after 100 cycles at 50 mA g^{-1} and 202 mAh g^{-1} at 500 mA g^{-1} even after 3200 cycles. In addition, we also calculate that pyridinic-N displays a smaller energy barrier of 0.16 eV compared to that of 1.12 eV for pyrrolic-N, indicating that pyridinic-N in carbon is the critical factor to improve the K-ion storage performance for our PANCs. Besides, the electrochemical impedance spectroscopy (EIS) and pseudocapacitance analysis also demonstrate that the increase of active N can greatly improve the K-ion diffusion ability. These features significantly contribute to the rapid interfacial K-ion adsorption reaction, leading to high discharge capacity and rate capability of PANCs when used for KIBs anodes.

2. Experimental

Synthesis

For the synthesis of PA-induced active-N-rich carbon nanosheets (PANC), a certain amount (1~3 mL) of phytic acid was dissolved in 50 mL 4 mg L^{-1} GO under stirring and ultrasonic treatment. After that, 10 mmol melamine (MEL, N source) and 100 mg polyvinyl pyrrolidone (PVP, K30) was added in the above solution with continuous stirring until the MEL was completely dissolved. Then mixed solution was transferred to hydrothermal treatment at 180 °C for 12 hours. After washing and freeze-drying process, the sample was calcined at 500 °C for 2 h with a heating rate of 3 °C min^{-1} under the Ar atmosphere to obtain the PANC composites.

Characterization

The morphologies of the samples were measured by a scanning electron microscope (SEM, Thermo Fisher (FEI) Helios G4 CX) and a transmission electron microscope (TEM, FEI talosf200s) with an energy spectrum (Talos 200S). The structures and surface properties were confirmed by X-ray diffraction (XRD, Rigaku), Raman spectrometer (horiba evolution), X-ray photoelectron spectroscopies (XPS, Thermo Fisher Scientific). The bulk composition of the PANC was measured using elemental analysis (EA) by Elementar Vario Micro cube analyzer. Nitrogen adsorption technique was carried out using a Micromeritics ASAP2460 instrument at a liquid nitrogen temperature to study the pore structures.

Electrochemical measurement

The electrochemical performances of the samples were measured using coin-type cells (CR2032). Metallic potassium foil for hall cell acted as counter electrode and glass fiber membrane (Whatman) was adopted as separator. 1 M potassium salt (potassium bis(fluorosulfonyl) imide, KFSI) in ethylene carbonate (EC) and propylene carbonate (PC) mixed solution with a volume ratio of 1:1 was used as electrolyte. Typically for work electrode, active material, Super P and sodium carboxymethyl cellulose was mixed with a ratio of 8:1:1 in water to form a homogeneous slurry. After that, the homogeneous slurry was coated on Cu foil and then dry in vacuum oven over night. The resulting electrode was cut into discs with a diameter of 14 mm and the batteries were assembled in an argon-filled (O$_2$<0.1 ppm, H$_2$O<0.1 ppm) glove box (Etelux, Lab2000). The galvanostatic charge-discharge curves were performed by the Neware battery test system (Neware, BTS-4000) in the range of 0.01-3.0 V for hall cell and 0.9-3.7 V for full cell. Cyclic voltammetry (CV) was recorded using ChenHua electrochemical workstation (CHI 1030C) at scan rate of 0.2 mV s^{-1} unless otherwise noted. Electrochemical impedance spectroscopies (EIS) were evaluated by Princeton electrochemical workstation (Veras STAT 3400). The DFT computational methods and diffusion coefficient calculated methods provided in supporting information section. The

3. Results and Discussions
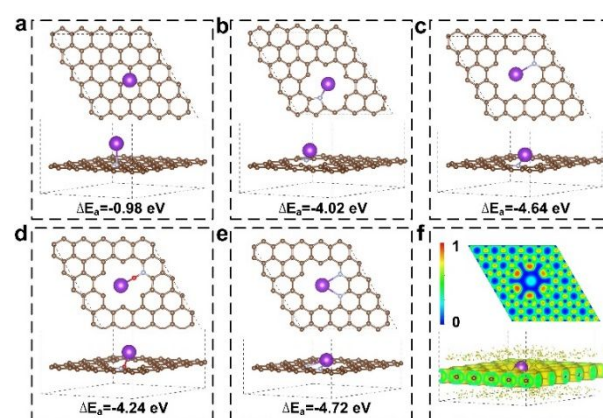
Figure 1. DFT calculations of the adsorption models: (a) graphitic-N, (b) pyrrolic-N, (c) pyridinic-N, (d) oxidized-N, (e) 2-pyridinic-N and (f) electronic localization function of 2-pyridinic-N-K. The brown, blue grey, red and blue-violet balls represent the C, N, O, and K atoms, respectively.

To investigate the mechanism of carbon with different N-configuration for K-ion storage, we calculated the ΔE$_a$ of carbon with different N doping site according to the DFT equation in the Surpporting Information. It is found that the graphitic-N, pyrrolic-N, pyridinic-N and oxidized-N sites in carbon present the ΔE$_a$ of -0.98, -4.02, -4.64 and -4.24 eV (Figure 1a~d, Table S1), respectively. A more negative ΔE$_a$ of pyridinic-N sites can be received, indicating that pyridinic-N sites will contributes a higher K-ion storage ability. To further investigate the N-configuration for K-ion storage, we also calculate the ΔE$_a$ of carbon with two pyridinic-N sites (2-pyridinic-N, Figure 1e), and we find that the ΔE$_a$ of 2-pyridinic-N increases to -4.72 eV, further confirming that the high pyridinic-N content can promote the K-ion storage performance. The side and top views of the electronic localization function of the 2-pyridinic-N model are calculated to understand the bonding characteristic of the doping-N atoms in depth (Figure 1f and Figure S1). After N doping, the degree of electron localization in this area is significantly reduced, indicating that an easier electron transfer process will occur. In addition, pyridinic-N and 2-pyridinic-N present lower degree of electron localization, indicating that more pyridinic-N contributes to the improvement of the K-ion transfer.
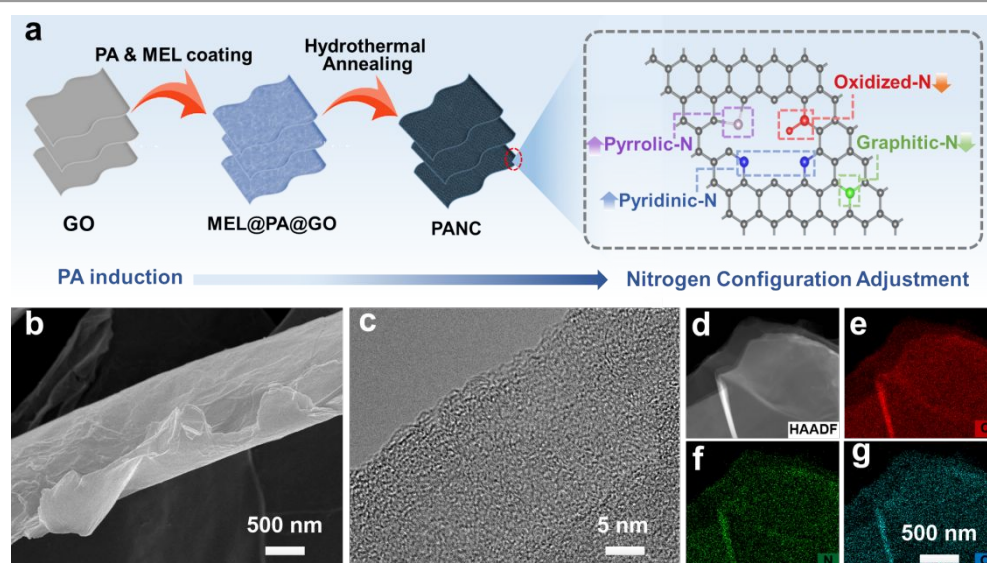
Figure 2. The synthesis process, the morphology and element distribution: (a) synthetic schematic, (b) SEM image, (c) TEM image and (d~g) elementic mapping of PANC-2.

According to the above DFT calculation, we suggest that designed N-doping carbon with high pyridinic-N configuration content will remarkably enhance the K-ion storage performance of carbon-based materials. Therefore, we attempt to use PA as inductive agent to realize the design of high proportion of active-N carbon nanosheets (PANC) with high pyridinic-N configuration content. Figure 2a shows the synthesis process of the PANC composite. In the process of synthesis, a certain amount of PA and melamine (MEL) with polyvinylpyrrolidone are adsorbed on the surface of graphene oxide (GO) via chelation to form MEL@PA@GO precursor. Afterwards, the MEL@PA@GO precursor undergoes hydrothermal and subsequent annealing treatment to obtain our PANC. The samples obtained by 1, 2 and 3 mL PA inductive agent in precursor are named as PANC-1, PANC-2 and PANC-3, respectively. Figure 2b~g show the morphology and element distribution of PANC-2. From the scanning electron microscopy (SEM) image in Figure 2b, it is found that the PANC-2 is constituted by the large flakes with a thickness of 10 nm. Such nanosheets structure in PANC-2 is conducive to exposing more active sites, which facilitates the adsorption of K-ions during potassiation-depotassiation process.[26-28] Figure S2 shows the SEM images of PANC-1 and PANC-3, indicating that the introduction of PA in precursor presents little effect on their morphology. The structure details of the PANC-2 are further confirmed by the transmission electron microscope (TEM) image, as shown in Figure 2c. Inconspicuous lattice fringes displayed in Figure 2c show the messy ordering of the carbon layers, which is also beneficial to the potassiation-depotassiation reaction.[29-31] The elemental mapping images confirm that the C, N and O elements are evenly distributed in the PANC-2, as shown in Figure 2d~g. For comparison, we also synthesize the N-doping carbon nanosheets without phytic acid (NC), reduced graphene oxide (RGO) and N-doping carbon composite without GO (PN) separately, the corresponding SEM

image and X-ray diffraction (XRD) patterns show in Figure S3 and S4. Figure S5 shows the X-ray diffraction (XRD) patterns of PANCs, which prove that our PANC samples are amorphous carbon. In addition, two sharp Raman peaks of all the samples located at 1350 and 1593 cm^{-1} can be observed, which are attributed to the D and G bands of PANCs, respectively (Figure S6). No significant change of the intensity ratios of D and G bands in these electrodes, indicating that the content of PA
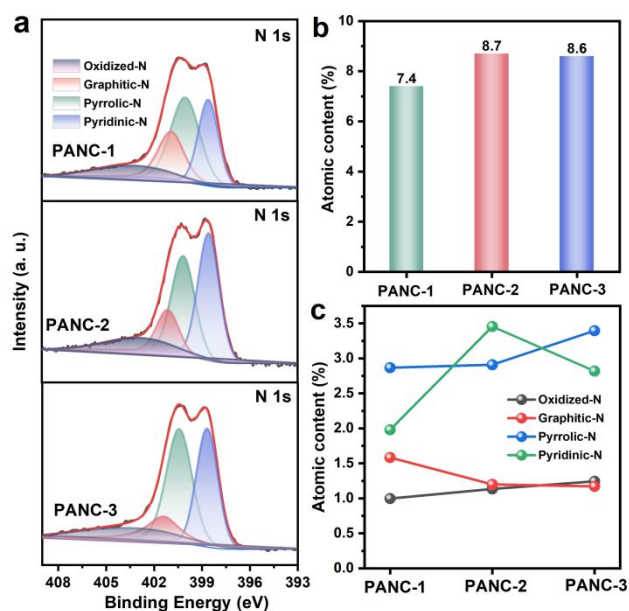
Figure 3. (a) high-resolution N 1s XPS spectra of PANCs after deconvoluting into pyridinic-N, pyrrolic-N, graphitic-N, and oxidized-N species, (b) the atomic contents of N 1s of PANCs, (c) the atomic contents of pyridinic-N, pyrrolic-N, graphitic-N and oxidized-N in PANC-1, PANC-2 and PANC-3 derived from the XPS results.

inductive agent in precursor present no obvious effect on the structure of PANCs. Figure S7 shows the N_2 adsorption-desorption isotherms and pore size distribution of PANCs. It is found that specific surface area of PANCs increase with the increase of PA inductive agent in precursor.

To confirm the regulation effect of PA on N-doping in PANCs, we provide the X-ray photoelectron spectroscopy (XPS) to analyse. Figure S8 shows the survey XPS spectra of PANCs, which demonstrate that the N has been doped successfully. To further investigate the variation of different doping N configuration, we provide the high-resolution N 1s XPS spectra of the PANCs (Figure 3a). Four typical N peaks located at 398.5, 400.1, 401.1 and 402.9 eV can be deconvolved, which correspond to pyridinic-N, pyrrolic-N, graphitic-N and oxidized-N in PANCs.[32, 33] From the XPS survey spectra, we obtained the N content of 7.4 at% 8.7 at% and 8.6 at% for PANC-1, PANC-2 and PANC-3 (Figure 3b), demonstrating their N-rich features. These high N doping content of PANCs are expected to effectively alter the electronic structure and facilitate the K-ion adsorption.[34] To confirm the atomic contents of pyridinic-N, pyrrolic-N, graphitic-N, and oxidized-N species in PANCs, we compared with the peak areas of each N species. Besides, we also obtained the atomic content of pyridinic-N, pyrrolic-N, graphitic-N and oxidized-N for PANC-1, PANC-2 and PANC-3 (Figure 3c) according to the above results. It is found that the pyridinic-N of PANC-1, PANC-2 and PANC-3 first significantly increases from 1.98 at% to 3.46 at%, and then decreases to 2.82 at%. The pyrrolic-N and oxidized-N increase from 2.87 to 3.40 at% and from 1.00 to 1.24 at% with the increase of PA inductive agent. In addition, a decrease graphitic-N content from 1.58 to 1.17 at% can be delivered from PANC-1 to PANC-3. From these results, we suggest that the pyridinic-N-rich carbon nanosheets can be modified by virtue of the PA inductive agent content. And the high pyridinic-N carbon nanosheets may facilitate the performance improvement during the electrochemical reaction. In brief, our method provides a controllable and effective approach for selectively modifying the N configuration on carbon materials. It is expected to serve as a decent material platform for studying the structure-activity relation of N-doped carbon potassium storage material at atomic level.

To evaluate the electrochemical properties of the PANC electrodes, we firstly compare with their initial galvanostatic charge-discharge and cyclic voltammetry curves, as shown in Figure 4a. All the electrodes present an irreversible cathode capacity at low voltage range in the initial discharge curve, which derives from the irreversible formation of the solid-electrolyte interphase (SEI) layer.[35-37] From the second cycle onward, no significant changes are observed, indicating superior stability and high reversibility of our PANC electrodes. Unsurprisingly, the PANC-2 anode presents the highest specific charging capacity due to the highest pyridine nitrogen content in the three electrodes. We suggest that the high K-ion storage
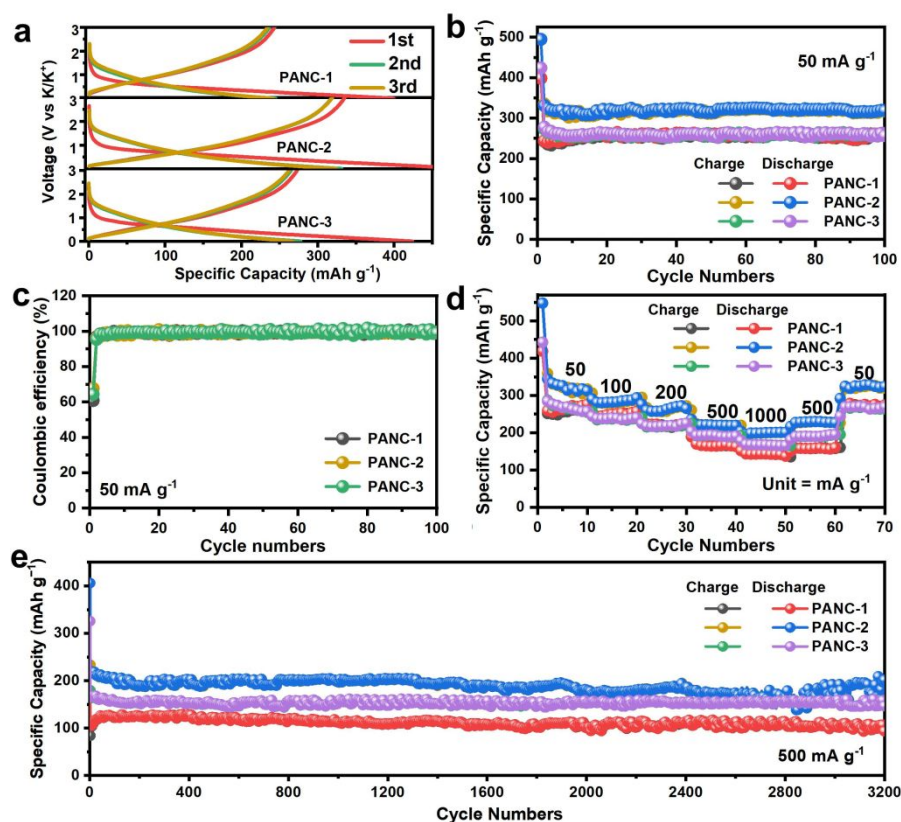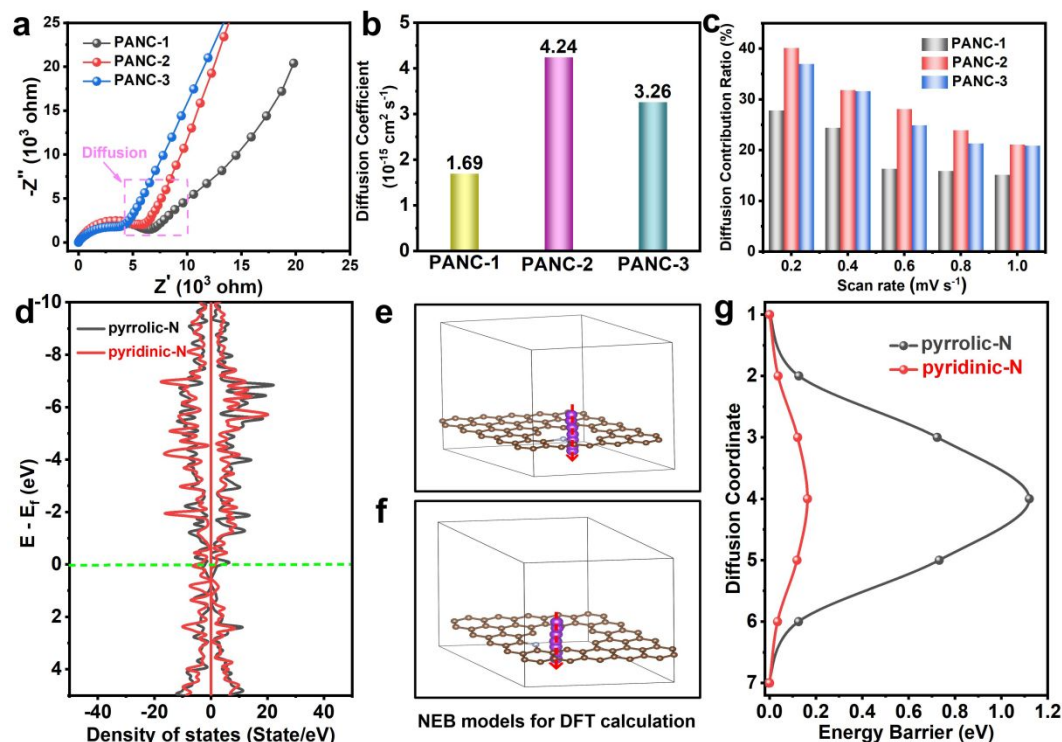

Figure 4. (a) Galvanostatic discharge/charge curves, (b) cycling performance, (c) Coulombic efficiency, (d) rate performance and (e) long-term cycling performance of PANC electrodes.

performance is closely involved into the N configuration in PANCs. To confirm the cycle stability, we also provide the cycling performance of our PANC electrodes at 50 mA g^{-1}, as shown in Figure 4b. Overall, all the three electrodes have high cycle stability, while the PANC-2 presents the highest reversible specific capacity of 317 mAh g^{-1} after 100 cycles, significantly higher than those of PANC-1 (reversible specific capacity of 257 mAh g^{-1} after 100 cycles) and PANC-3 (reversible specific capacity of 259 mAh g^{-1} after 100 cycles). Figure 4c shows the Coulombic efficiencies of the electrodes. It is found that PANC-2 also present a higher initial Coulombic efficiency of 68% compared with those in PANC-1 (61%) and PANC-3 (64%). In the subsequent cycles, all the electrodes present the high Coulombic efficiency over 99.5%, indicating a high reversibility of our PANC electrodes. In addition, we also optimize the annealing temperature of PANC electrodes, as shown in Figure S9. It is found that the PANC-2 electrode annealing at 500 °C presents the optimal K-ion storage performance. The K-ion storage performance of NC, RGO and PN are also provided in Figure S10. The Figure 4d presents the rate performances of the electrodes. Consistent with Figure 4a~b, the PANC-2 displays the best performance between these three electrodes. In particular, the PANC-2 electrode delivers a reversible specific capacity of 317, 295, 261, 220 and 201 mAh g^{-1} at 50, 100, 200, 500 and 1000 mA g^{-1}, respectively. When the current density returns to 500 and 50 mA g^{-1}, the reversible specific capacity can also recover to 226 and 320 mAh g^{-1}. Furthermore, we also

provide the long-term cycling performance of our PANC electrodes in Figure 4e. The PANC-2 electrode still receives a high specific capacity of 202 mAh g^{-1} at 500 mA g^{-1} after 3200 cycles, with a capacity retention rate of 86%, which is much higher than those of PANC-1 and PANC-3 electrodes.

To further understand the kinetic features of the PANCs in KIBs, the EIS profiles are applied to measure the diffusion coefficient of K-ion in the electrodes (Figure 5a, b). As shown in Figure 5a and S11, all the EIS profiles exhibit a semicircle in the high-frequency region and a straight line in the low-frequency region. The wide semicircle in the high frequency region represents the charge-transfer resistance, while the straight line in the low frequency region is related to the Warburg resistance for K-ion diffusion through PANCs.[38, 39] It is found that the impedance of electrodes in the high-frequency region gradually decrease with the increase of PA in precursor. We suggest that the N content and species can change the charge transfer behavior. In addition, the diffusivity coefficient of K-ions can be calculated according to Fick's second law using the simplified equation in the Supporting Information. And the calculation results are shown in the Figure 5b. Obviously, the PANC-2 electrode has a relatively higher diffusion coefficient (4.24×10^{-15} cm^2 s^{-1}), compared with the PANC-1 electrode (1.69×10^{-15} cm^2 s^{-1}) and the PANC-3 electrode (3.26×10^{-15} cm^2 s^{-1}). To further explore the dynamic behavior of the PANC electrodes for K-ion storage, the CV curves at the scan rates from 0.2 to 1.0 mV s^{-1} of our PANCs in KIBs are analyzed (Figure 5c, S12). The

Figure 5. (a) Galvanostatic discharge/charge curves, (b) cycling performance, (c) Coulombic efficiency, (d) rate performance and (e) long-term cycling performance of PANC electrodes.

surface-driven process contribution could be quantitatively differentiated using the following equation:

$$i = k_1v + k_2v^{1/2} \tag{1}$$

where i is the current at a fixed potential, v represents the scan rate in the CV tests, and the k_1 and k_2 are constants.[40] The k_1v and $k_2v^{1/2}$ are supposed to the capacitive and diffusion-controlled processes, respectively.[41] Generally, based on the Dunn's method,[42-44] the contributions from the diffusion-controlled storage for PANCs at different scan rates are characterized (Figure 5c). Generally, diffusion-controlled charges at various scan rates (0.2 to 1.0 mV s⁻¹) for the PANC-2 are higher than those for PANC-1 and PANC-2. These results again illustrate that the increase of active N presents an important impact on the improvement of the diffusion ability, thus contributing to the better K-ion storage performance. To further compare the kinetic property of pyrrolic-N and pyridinic-N in PANCs, we also calculate total density of states (DOS) and the energy barrier for K-ion diffusion of pyrrolic-N and pyridinic-N in Figure 5d~g. It can be observed clearly that the electron density states of these two N-doped carbon cross the Fermi surface in Figure 5d, indicating that they are conductors with similar conductivity.[45] The dynamics of K-ion diffusion for both electrode materials are simulated via the climbing image nudged elastic band (CI-NEB) method.[46] The calculated K-ion migration pathways are exhibited in Figure 5e and 5f. It is found that the pyridinic-N displays a smaller energy barrier of 0.16 eV compared to the energy barrier of pyrrolic-N (1.12 eV), as shown in Figure 5g and Table S2. The calculation results also show that the diffusion ability of pyridine-N-doped carbon materials is significantly improved, which is very important to improve the K-ion storage performance.[47]

Figure 6. Demonstration of K-ion full battery: (a) the lighted blue LED panel driven by the full battery, (b) diagram illustration of the full cell, (c, d) galvanostatic charge/discharge curves of FeHCF and PANC at 50 mA g⁻¹, (e, f) galvanostatic charge/discharge curves and the cycling performance of the full battery at 50 mA g⁻¹.

To validate the practical application of our PANC anode, the K-ion full cell is fabricated with KFe[Fe(CN)₆] (FeHCF) as cathode electrode.[48] The KIB panel with 48 blue light emitting diodes (LEDs) can be lighted by the K-ion full battery (Figure 6a and S13), proving the feasibility of the low-cost K-ion storage device based on the structure of the diagrammatic drawing in Figure 6b. Before assembling the full cell, the FeHCF and PANC electrodes should be activated to remove the large first irreversible capacity and supplement sufficient K-ions for

intercalation/deintercalation during cycling (Figure 6c and 6d). Figure 6e shows the charge/discharge profiles of FeHCF//PANC K-ion full battery. A high voltage plateau can be obtained, indicating that our PANC electrode is ideal for KIB's anode. Figure 6f shows cycling performance of FeHCF//PANC K-ion full battery. It is found that our full battery delivers an ideal charge capacity of 57 mAh g⁻¹ at 50 mA g⁻¹, and a high reversible capacity of 52 mAh g⁻¹ with a capacity retention of 91.2% after 15 cycles, suggesting high electrochemical reversibility as well as fast electron and K-ion transfer ability between cathode and anode.

4. Conclusions

In summary, we have successfully prepared the PANCs by PA induction for K-ion storage. Under the effect of appropriate PA, the pyridinic-N content of PANCs can be improved from 1.98 at% to 3.46 at%. Such high pyridinic-N content of PANC possesses a high capacities of 317 mAh g⁻¹ after 100 cycles at 50 mA g⁻¹, and 202 mAh g⁻¹ at 500 mA g⁻¹ even after 3200 cycles. It is revealed by analyzing the K-ion adsorption and diffusion abilities that the pyridinic-N is more conducive to the improvement of K-ion storage performance according to DFT calculations. Furthermore, the improvement of diffusion ability has been further confirmed by EIS and pseudocapacitance analysis. In brief, our work will offer a reference for active N doping of carbon anode materials for KIBs, which also provide an in-depth understanding involving the electrochemical behaviors of carbon composite with high pyridinic-N content.
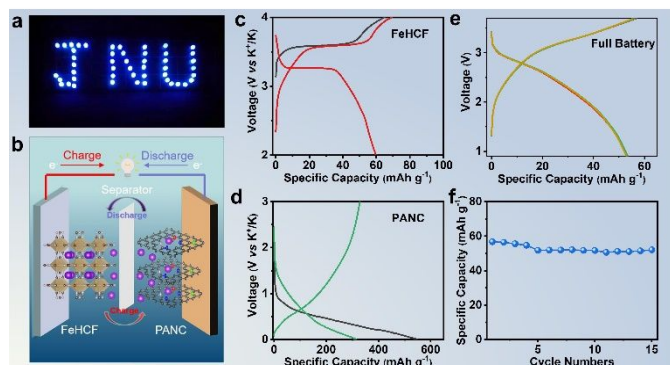
Conflicts of interest

There are no conflicts of interest to declare

CRediT

Liang Ma and **Zhibin Li**: Conceptualization, Methodology, Writing-original draft; **Yao Dai**: Validation; **Chen Qian** and **Mohammed A. Amin**: Methodology; **Yaofeng Zhu**: Representation; **Hao Wang**: Resources and Methodology; **Kwun Nam Hui** and **Likun Pan**: Supervision; **Jinliang Li**, **Yusuke Yamauchi** and **Wenjie Mai**: Investigation, Supervision, Resources and Writing-final draft.

Acknowledgements

References

1. Y. Zhu, J. Xie, A. Pei, B. Liu, Y. Wu, D. Lin, J. Li, H. Wang, H. Chen, J. Xu, A. Yang, C. L. Wu, H. Wang, W. Chen and Y. Cui, *Nat Commun*, 2019, **10**, 2067.
2. X. Li, J. Li, L. Ma, C. Yu, Z. Ji, L. Pan and W. Mai, *Energy Environ. Mater.*, 2021, 10.1002/eem1002.12194.
3. Y. Xie, Y. Chen, L. Liu, P. Tao, M. Fan, N. Xu, X. Shen and C. Yan, *Adv. Mater.*, 2017, **29**, 1702268.
4. R. Hao, H. Lan, C. Kuang, H. Wang and L. Guo, *Carbon*, 2018, **128**, 224-230.
5. X. Li, X. Yang, H. Xue, H. Pang and Q. Xu, *EnergyChem*, 2020, **2**, 100027.
6. K. Lei, F. Li, C. Mu, J. Wang, Q. Zhao, C. Chen and J. Chen, *Energy Environm. Sci.*, 2017, **10**, 552-557.
7. V. Gabaudan, R. Berthelot, L. Stievano and L. Monconduit, *J. Phys. Chem. C*, 2018, **122**, 18266-18273.
8. S. Gong and Q. Wang, *J. Phys. Chem. C*, 2017, **121**, 24418-24424.
9. K. C. Wasalathilake, G. A. Ayoko and C. Yan, *Carbon*, 2018, **140**, 276-285.
10. Y. Qian, Y. Li, Z. Yi, J. Zhou, Z. Pan, J. Tian, Y. Wang, S. Sun, N. Lin and Y. Qian, *Adv. Funct. Mater.*, 2020, **31**, 2006875.
11. X. Hu, Y. Liu, J. Chen, L. Yi, H. Zhan and Z. Wen, *Adv. Energy Mater.*, 2019, **9**, 1901533.
12. J. Li, W. Qin, J. Xie, H. Lei, Y. Zhu, W. Huang, X. Xu, Z. Zhao and W. Mai, *Nano Energy*, 2018, **53**, 415-424.
13. X.-R. Han, X.-T. Guo, M.-J. Xu, H. Pang and Y.-W. Ma, *Rare Metals*, 2020, **39**, 1099-1106.
14. Y. Xu, C. Zhang, M. Zhou, Q. Fu, C. Zhao, M. Wu and Y. Lei, *Nat. Commun.*, 2018, **9**, 1720.
15. X. Chang, X. Zhou, X. Ou, C. S. Lee, J. Zhou and Y. Tang, *Adv. Energy Mater.*, 2019, **9**, 1902672.
16. H. Tong, C. Wang, J. Lu, S. Chen, K. Yang, M. Huang, Q. Yuan and Q. Chen, *Small*, 2020, **16**, 2002771.
17. L. Ma, J. Li, Z. Li, Y. Ji, W. Mai and H. Wang, *Nanomaterials*, 2021, **11**, 1130.
18. Z. Ju, P. Li, G. Ma, Z. Xing, Q. Zhuang and Y. Qian, *Energy Storage Mater.*, 2018, **11**, 38-46.
19. P. Li, J.-Y. Hwang, S.-M. Park and Y.-K. Sun, *J. Mater. Chem. A*, 2018, **6**, 12551-12558.
20. Y. Li, C. Yang, F. Zheng, X. Ou, Q. Pan, Y. Liu and G. Wang, *J. Mater. Chem. A*, 2018, **6**, 17959-17966.
21. J. Liu, T. Yin, B. Tian, B. Zhang, C. Qian, Z. Wang, L. Zhang, P. Liang, Z. Chen, J. Yan, X. Fan, J. Lin, X. Chen, Y. Huang, K. P. Loh and Z. X. Shen, *Adv. Energy Mater.*, 2019, **9**, 1900579.
22. L. Li, C. Tang, Y. Zheng, B. Xia, X. Zhou, H. Xu and S. Z. Qiao, *Adv. Energy Mater.*, 2020, **10**, 2000789.
23. H. Song, M. Wu, Z. Tang, J. S. Tse, B. Yang and S. Lu, *Angew.Chem. Int. Ed.*, 2021, **60**, 7234–7244.
24. J. Niu, J. Guan, M. Dou, Z. Zhang, J. Kong and F. Wang, *ACS Appl. Energy Mater.*, 2020, **3**, 2478-2489.
25. K. Li, Z. Hu, J. Ma, S. Chen, D. Mu and J. Zhang, *Adv. Mater.*, 2019, **31**, 1902399.
26. T. Peng, Z. Tan, M. Zhang, L. Li, Y. Wang, L. Guan, X. Tan, L. Pan, H. Fang and M. Wu, *Carbon*, 2020, **165**, 296-305.
27. H. Wang, L. Wang, L. Wang, Z. Xing, X. Wu, W. Zhao, X. Qi, Z. Ju and Q. Zhuang, *Chem. Eur. J.*, 2018, **24**, 13897-13902.
28. D. Adekoya, M. Li, M. Hankel, C. Lai, M.-S. Balogun, Y. Tong and S. Zhang, *Energy Storage Mater.*, 2020, **25**, 495-501.
29. S. Zeng, X. Chen, R. Xu, X. Wu, Y. Feng, H. Zhang, S. Peng and Y. Yu, *Nano Energy*, 2020, **73**, 104807.
30. J. Wang, J. Yuan, C. Chen, L. Wang, Z. Zhai, Q. Fu, Y. Liu, L. Dong, W. Yan, A. Li and J. Zhang, *Nano Energy*, 2020, **75**, 104914.
31. Y. Qian, S. Jiang, Y. Li, Z. Yi, J. Zhou, J. Tian, N. Lin and Y. Qian, *Energy Storage Mater.*, 2020, **29**, 341-349.
32. T. Xing, Y. Zheng, L. H. Li, B. C. C. Cowie, D. Gunzelmann, S. Z. Qiao, S. Huang and Y. Chen, *ACS Nano*, 2014, **8**, 6856–6862.
33. C. Tang, H. F. Wang, X. Chen, B. Q. Li, T. Z. Hou, B. Zhang, Q. Zhang, M. M. Titirici and F. Wei, *Adv. Mater.*, 2016, **28**, 6845-6851.
34. J. Ruan, X. Wu, Y. Wang, S. Zheng, D. Sun, Y. Song and M. Chen, *J. Mater. Chem. A*, 2019, **7**, 19305-19315.
35. W. Hong, Y. Zhang, L. Yang, Y. Tian, P. Ge, J. Hu, W. Wei, G. Zou, H. Hou and X. Ji, *Nano Energy*, 2019, **65**, 104038.
36. J. Ruan, Y. Zhao, S. Luo, T. Yuan, J. Yang, D. Sun and S. Zheng, *Energy Storage Mater.*, 2019, **23**, 46-54.
37. Q. Sun, D. Li, J. Cheng, L. Dai, J. Guo, Z. Liang and L. Ci, *Carbon*, 2019, **155**, 601-610.
38. Z. Xu, Z. Du, S. Yi, J. Han, C. Lai, Y. Xu and X. Zhou, *ACS Appl. Energy Mater.*, 2020, **3**, 11410-11417.
39. S. Zheng, Q. Li, H. Xue, H. Pang and Q. Xu, *Natl. Sci. Rev.*, 2019, **7**, 305-314.
40. W. Yang, J. Zhou, S. Wang, Z. Wang, F. Lv, W. Zhang, W. Zhang, Q. Sun and S. Guo, *ACS Energy Lett.*, 2020, **5**, 1653-1661.
41. B. Lee, M. Kim, S. Kim, J. Nanda, S. J. Kwon, H. D. Jang, D. Mitlin and S. W. Lee, *Adv. Energy Mater.*, 2020, **10**, 1903280.
42. J. Wang, J. Polleux, J. Lim and B. Dunn, *J. Phys. Chem. C*, 2007, **111**, 14925-14931.
43. T. Brezesinski, J. Wang, S. H. Tolbert and B. Dunn, *Nat. Mater.*, 2010, **9**, 146-151.
44. J. B. Cook, H. S. Kim, Y. Yan, J. S. Ko, S. Robbennolt, B. Dunn and S. H. Tolbert, *Adv. Energy Mater.*, 2016, **6**, 1501937.
45. B. Wang, F. Yuan, W. Li, Q. Wang, X. Ma, L. Gu, H. Sun, K. Xi, D. Zhang and W. Wang, *Nano Energy*, 2020, **75**, 104979.
46. P. Liu, Y. Wang, Q. Gu, J. Nanda, J. Watt and D. Mitlin, *Adv Mater*, 2020, **32**, e1906735.
47. J. Yang, Y. Zhai, X. Zhang, E. Zhang, H. Wang, X. Liu, F. Xu and S. Kaskel, *Adv. Energy Mater.*, 2021, 2100856.
48. W. Zhuo, J. Li, X. Li, L. Ma, G. Yan, H. Wang, S. Tan and W. Mai, *Surf. Interf.*, 2021, **23**, 100911.